Polarized Light Imaging of White Matter Architecture

LUIZA LARSEN,[1] LEWIS D. GRIFFIN,[1] DAVID GRÄßEL,[2,3] OTTO W. WITTE,[2] AND HUBERTUS AXER[2]*
[1]*Department of Computer Science, University College London, London WC1E 6BT, United Kingdom*
[2]*Department of Neurology, Friedrich-Schiller-University Jena, D-07747 Jena, Germany*
[3]*Institute of Diagnostic and Interventional Radiology, Friedrich-Schiller-University Jena, D-07747 Jena, Germany*

KEY WORDS PLI; fiber tracts; polarized light physics; birefringence; crossed polars; postmortem; human; rat; brain

ABSTRACT Polarized light imaging (PLI) is a method to image fiber orientation in gross histological brain sections based on the birefringent properties of the myelin sheaths. The method uses the transmission of polarized light to quantitatively estimate the fiber orientation and inclination angles at every point of the imaged section. Multiple sections can be assembled into a 3D volume, from which the 3D extent of fiber tracts can be extracted. This article describes the physical principles of PLI and describes two major applications of the method: the imaging of white matter orientation of the rat brain and the generation of fiber orientation maps of the human brain in white and gray matter. The strengths and weaknesses of the method are set out. *Microsc. Res. Tech. 70:851–863, 2007.*

INTRODUCTION

The two main tissue classes of the human central nervous system (CNS) are gray and white matter. These tissue classes are the substrate of the short- and long-range connectivity of the CNS, respectively. The gray matter contains the cell bodies of neurons and a profusion of short-range (of the order of millimeters or less) connections. An apt visual analogy for this tissue is that of leafless trees, so densely planted that their crowns intersect and overlap (Griffin, 1994). The white matter consists of a mass of intermingled unbranching nerve fibers that are the long-range axonal projections of the neurons in the gray matter to other regions of gray matter. The function of these axonal projections is to convey neural activity from one gray matter structure (e.g., cortical area) to others with related function. Some projections are between adjacent structures (giving rise to "u-fiber bundles") and so are relatively short-range (centimeters), while others such as interhemispheric and cortico-spinal fibers link more distant structures. The white matter projections link the neural networks of individual cortical areas into large-scale networks that are able to realize complex neuropsychological tasks such as language, attention, and perception (Mesulam, 1990). Therefore, mapping the three-dimensional anatomical architecture of the white matter will give insight into the logical functional architecture of neurocognitive processes.

Recently, the development of Diffusion Tensor Magnetic Resonance Imaging (DT-MRI) has led to an increased interest in CNS connectivity. DT-MRI is a technique that measures water diffusion in the living human brain (Basser et al., 1994; Beaulieu, 2002). In white matter, the locally ordered structure of parallel-packed fibers gives rise to anisotropic diffusion: diffusion is faster in the direction along the fibers than perpendicular to them. Thus, DT-MRI measurements of the spatially varying diffusivity tensor provide information about the spatially varying orientation of fiber tracts in the white matter of the brain. DT-MRI is becoming an important tool for the study of brain anatomy and white matter pathology (Jones et al., 2001; Wakana et al., 2004).

There is a need to validate the use of DT-MRI as a method of measuring white matter architecture. This need is pressing for two reasons. The first is that DT-MRI is being used in an indirect and inferential manner and so requires validation like any such measurement method. The second is that, although from DT-MRI it is only possible to infer *local* information about fiber orientation, the results are being integrated across space to infer long-range fiber connectivity. This process of integrating local orientation data is numerically precarious because, although random errors may be tolerated, systematic inaccuracies are likely to be amplified.

A new approach to the validation of DT-MRI is through the use of polarized light imaging (PLI) which has been developed to acquire directional information on fiber tracts in gross histological sections (Axer et al., 2001). Although the first descriptions of this new method have given some information about the experimental and empirical development of the method, for a rather technical audience of medical physicists a comprehensive and detailed description of PLI physics is still missing. Thus, the main goal of this article is a review of the physical principles of PLI. Some equipment configurations for performing PLI on brain sections are described, and some results of imaging mouse

*Correspondence to: Hubertus Axer, Department of Neurology, Friedrich-Schiller-University Jena, Erlanger Allee 101, D-07747 Jena, Germany.
E-mail: hubertus.axer@med.uni-jena.de

Received 23 February 2007; accepted in revised form 3 April 2007

Contract grant sponsor: DFG (Deutsche Forschungsgemeinschaft; Contract grant number: Ax 20/3-1.

DOI 10.1002/jemt.20488

Published online 27 July 2007 in Wiley InterScience (www.interscience.wiley.com).

and human brain to image fiber orientation in the white and the gray matter. The advantages and disadvantages of PLI are discussed.

MATERIALS AND METHODS

Polarization

Electromagnetic radiation propagates as a wave. The wave is of the transverse type meaning that its oscillations are orthogonal to the direction of propagation. A light beam from a source such as a filament is said to be unpolarized as the direction of oscillation varies moment-to-moment in an unpredictable manner. In contrast, the direction of oscillation of a polarized beam varies over time in a smooth lawful manner. There are various states of polarization. At one extreme is plane polarization where all oscillations are in the same plane; at the other extreme is circular polarization where the direction of oscillation rotates at constant speed around the direction of propagation; intermediate between the two is elliptical polarization. Conveniently, the behavior of the different states of polarization can be analyzed uniformly by taking advantage of the fact that any polarized beam is identical to the superimposition of a pair of beams that are: (i) polarized in planes that are perpendicular and contain the direction of propagation; and (ii) have appropriately chosen amplitudes and phase difference between them. In fact, such an identity can be found uniquely for any pair of perpendicular planes.

Refractive Index

When a light wave passes through a medium it interacts with the dipoles of the medium, causing it to propagate more slowly than through vacuum. This effect is quantified by the medium-dependent refractive index (RI), which is defined to be the speed through vacuum divided by the speed through the medium. RI is referred as n. Typical RIs for biological tissues are 1.38 for muscle (Haskell et al., 1989), 1.40 for chicken liver, 1.46 for unfixed neurons (de Campos Vidal et al., 1980), 1.47 for porcine adipose tissue (Lai et al., 2005), 1.48 for lipids (Beuthan et al., 1996), and 1.55 for collagen (Turner et al., 2000).

If the medium is isotropic at the scale of the wavelength of the light, then the RI will be independent of the direction of propagation and of the state of polarization of the light. However, if the medium is anisotropic at the scale of the wavelength of the light, then the RI will vary depending on the direction of propagation of the light wave and the state of its polarization. This orientation dependency can cause the polarization state of a beam to be changed by passage through the medium. A material that exhibits such dependency is said to be birefringent.

Birefringence

If a birefringent medium is homogenous at the scale of the wavelength of the light then the dependency of the RI on the direction of propagation and state of polarization is necessarily simple. Dependent on the medium and how it is orientated in the world, one can always find a coordinate system $\langle u, v, w\rangle$ so that the RI encountered by a general propagating plane-polarized wave, oscillating (perpendicular to the direction of propagation) in a direction specified by a unit vector $\vec{d} = (d_u\ d_v\ d_w)^T$ is given by $n_{\vec{d}} = (d_u^2 n_{uu}^{-2} + d_v^2 n_{vv}^{-2} + d_w^2 n_{ww}^{-2})^{-1/2}$ (Fig. 1). A plane polarized beam that is propagating in the direction of one of the coordinate axes (e.g., x), and is oscillating in the direction of another of the axes (e.g., y) will encounter only a single RI (n_{yy} in the example) and will propagate at the appropriate speed ($n_{yy}^{-1}c$) with an unchanging polarization state. Other beams will experience a nonextremal RI which leads (via Fermat's principle) to splitting of the beam and changes in polarization.

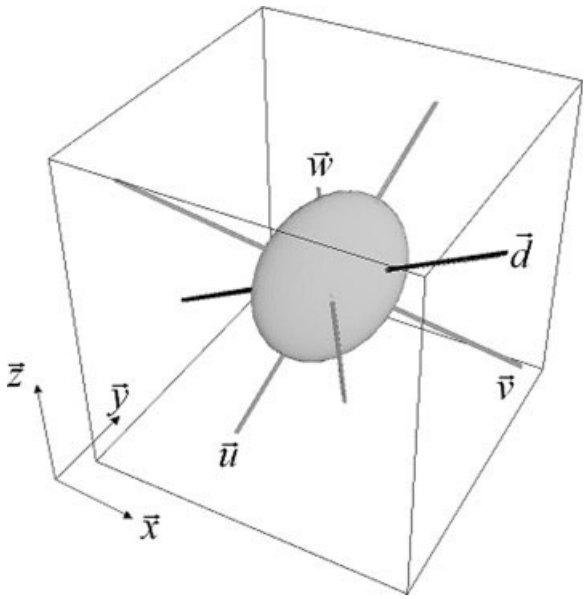

Fig. 1. RI indicatrix of a general birefringent medium. Note the difference between world coordinates $\langle x,y,z\rangle$ and the coordinate system $\langle u,v,w\rangle$ specially aligned to the medium. The indicatrix has the form of a tri-axial ellipsoid. The distance of a point of the indicatrix from the origin indicates the RI for oscillations in that direction. The RI has extremal values for directions along the principal axes (i.e., $\vec{u}, \vec{v}, \vec{w}$) of the indicatrix. For other directions (e.g., $\vec{d}$) the RI has intermediate values.

Birefringence of a Thin Section

Birefringent media are of two possible types—biaxial where all three of the RIs are different and uni-axial where two of the three RIs are the same. Uni-axial media have the same RI in all directions within a certain plane of symmetry, but a different RI in an axial direction orthogonal to the symmetry plane. If the axial RI is the smaller, the birefringence is said to be negative, otherwise positive. Whatever the type, the birefringence of a thin section of a birefringent medium requires only two refractive indices to be described. In a suitable coordinate system, the RI is given by $n_{\vec{d}} = (d_a^2 n_{aa}^{-2} + d_b^2 n_{bb}^{-2})^{-1/2}$ (Fig. 2).

A plane polarized beam, normally incident on the section described above, vibrating in the a- or b-direction will encounter only a single RI and so will not have its polarization state changed. To understand what happens to a plane polarized beam vibrating in a direction $\vec{d}$ making an angle θ relative to the a-axis we can use the decomposition property of polarized beams noted before. The single beam can be decomposed into

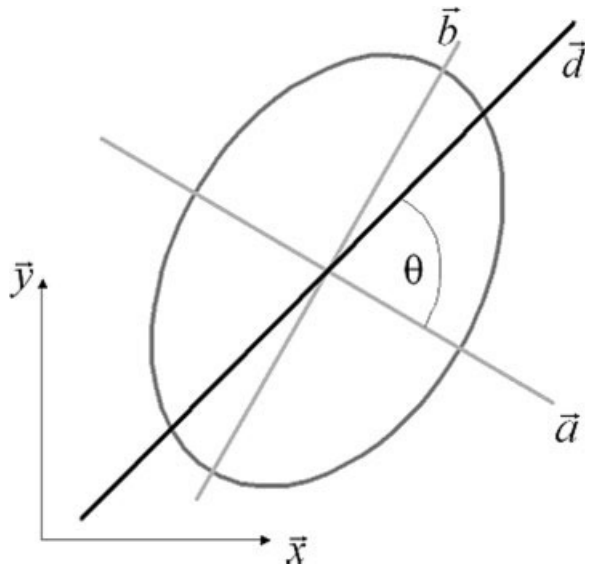

Fig. 2. RI indicatrix of a thin section of a general birefringent medium. The 2D indicatrix is elliptical because it is actually a slice through the ellipsoidal indicatrix of the 3D medium from which the thin section originates. As in Figure 1, note the difference between world coordinates $\langle x,y \rangle$ and the coordinate system $\langle a,b \rangle$ specially aligned to the birefringence of the thin section.

a beam of intensity $\cos^2\theta$ oscillating in the a-direction, and a beam of intensity $\sin^2\theta$ oscillating in the b-direction. Before passage through the section, the two constituent beams are oscillating in phase. Each of the constituent beams encounters an extremal RI and so there is no change to their individual polarization states, but the RIs encountered by the two beams are different and so they will no longer be in phase after passage through the medium. The phase difference is given by $\delta = 2\pi\lambda^{-1}t\,\Delta n$, where λ is the vacuum wavelength, t the section thickness, and $\Delta n = n_{aa} - n_{bb}$ is the difference between the refractive indices encountered by the two constituent beams. When the two beams are recombined, the phase difference between them means that the resulting beam will have the general, elliptically polarized form. Given a particular phase difference, what determines the degree to which the polarization of the resulting beam is elliptical rather than planar is the relative intensities of the two constituent beams. If the original beam was vibrating in a direction near the a- or b-direction, then one of the two constituent beams is of low intensity and so the polarization of the resulting beam is only mildly elliptical; but if the original vibration direction was intermediate between the u- and v-directions, the two constituent beams are of similar intensity, and so the polarization of the resulting beam is more elliptical.

Form Birefringence

Birefringence was first identified in crystals, where the orderly arrangement of atoms can give rise to anisotropy in the mobility of dipoles. The measurement of such molecular birefringence has been developed to a high degree of accuracy (Kaminsky et al., 2004) and is used for the identification of crystals and the understanding of their atomic structure (among many other uses).

Birefringence can also occur due to the orderly arrangement of units far larger than inorganic molecules. This type of "form birefringence" was first analyzed by Weiner (1912) who showed, for example, that a system of parallel rods occupying a volume fraction r in a medium would display uniaxial birefringence, with its two refractive indices (n_f for vibrations parallel to the rods, and n_c for vibrations normal to the rods) being related to the refractive indices of the nonbirefringent rods and medium (n_r, n_m) by $n_f^2 - n_c^2 = \frac{r(1-r)(n_r^2-n_m^2)^2}{(n_r^2+n_m^2)+r(n_m^2-n_r^2)}$. Note that the formula shows that the birefringence is negative (i.e., $n_f < n_c$) if and only if the RI of the rods is less than that of the medium. This formula also shows that form birefringence depends on the difference between refractive indices of the medium and the material in the medium (rods in the example above). Changing the RI of the medium to be the same as the material will cause the form birefringence to disappear (Wolman, 1975).

Typically, it is form birefringence that is present in biological samples, and its particular interest is that its measurement can be used to make quantitative inferences about geometrical structure that may be difficult or impossible to image microscopically (Gimpel et al., 1995; Glazer et al., 1996; Hoyt and Oldenbourg, 1999; Jin et al., 2003; Jouk et al., 1995; Oldenbourg and Mei, 1995; Richards, 1944; Scheuner and Hutschenreiter, 1972; Schmidt, 1924; Tower and Tranquillo, 2001; Wolman, 1975). However many biological samples, in addition to any form birefringence, also exhibit intrinsic birefringence caused by properties of the molecules they are composed of. The overall birefringence of the sample, called compound birefringence, depends on both form and intrinsic birefringence.

Birefringence of White Matter

The white matter of the mammalian brain consists of closely packed axonal fibers. The characteristic white color of the tissue is caused by the myelin content of sheaths that enclose axons larger than 1 μm in diameter. The sheaths are multilayer structures that substantially enhance the conduction speed of the enclosed axons. They are composed of radially ordered lipids (70–85%, e.g., cholesterol and sphingolipids) and proteins (15–30%, e.g., proteolipidprotein (PLP), myelin-associated glycoprotein (MAG), and myelin basic protein (MBP)) arranged tangentially to the axon. Although they enclose axons, the myelin sheaths are not actually part of the neurons whose axons lie in the white matter; rather they are parts of a type of glial cell known as an oligodendrocyte, each of which produces the myelin sheaths for 40 or more axons.

White matter exhibits negative uniaxial birefringence (Fraher and MacConaill, 1970; Göthlin, 1913; Kretschmann, 1967; Miklossy and Vanderloos, 1991; Schmidt, 1923; Schmitt and Bear, 1936; Wolman, 1970). Although the structure of white matter (parallel-packed fibers) is similar to the rods-in-medium model of form birefringence analyzed by Weiner (Weiner, 1912), and although there are a number of birefringent components within each axon (e.g., microtubules and neuro-filaments), the compound birefrin-

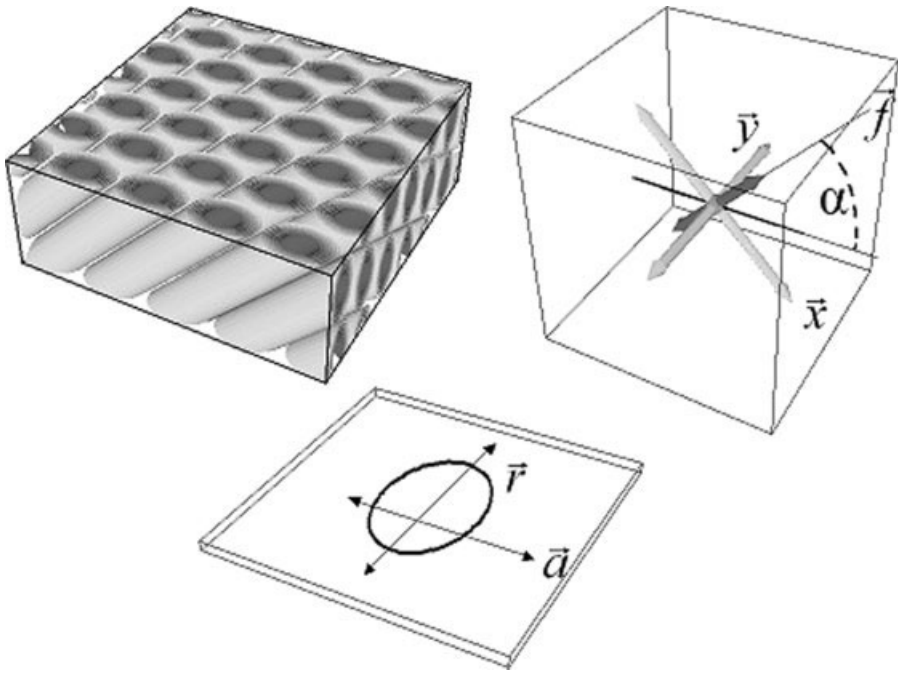

Fig. 3. Coordinate systems involved when imaging a thin section of white matter. Top left: an illustration of a thin section of white matter showing locally parallel-packed fibers. Top right: The thick arrows are proportional to the RIs for vibrations in these directions; the one for the fiber direction ($\vec{f}$) is shortest, and the ones for the other two directions ($\vec{x}$ and $\vec{y}$) are of equal length because white matter is a uniaxial negatively birefringent medium. Bottom: when considering only light passing normally through the section, the 3D system of RIs collapses to a 2D one. The RI in the within-section fiber direction ($\vec{a}$) is less than the RI in the cross-fiber direction ($\vec{r}$).

gence of white matter has been attributed to the regular arrangement of lipids in the myelin sheaths, rather than the geometry of individual white matter tissue components, which also exhibit birefringence (although much weaker). Measurements of birefringence before and after treatment (de Campos Vidal et al., 1980; Morell et al., 1989) have shown that the overall negative birefringence of white matter is due to the strong negative birefringence of the myelin content of the sheaths, weakened by the positive birefringence of the protein framework in which the myelin molecules sit.

For a block of vertically oriented fibers, the dependence of the RI on the direction of vibration has the form $n_{\vec{d}} = ((d_x^2 + d_y^2)n_{cc}^{-2} + d_z^2 n_{ff}^{-2})^{-½}$, where $n_{ff} < n_{cc}$ because the birefringence is negative. If this block is sectioned in a plane that the fiber axes make an angle α with, then the RI of the resulting thin section will be given by $n_{\vec{d}} = (d_r^2 n_{cc}^{-2} + d_a^2(n_{cc}^{-2} \sin^2 \alpha + n_{ff}^{-2} \cos^2 \alpha))^{-½}$ in a coordinate system where *a* is the axial direction along the projection of the fiber axis onto the section plane, and *r* is the orthogonal direction across the fiber axis (Fig. 3). The difference between the two refractive indices is $\Delta n = n_{cc} - (n_{cc}^{-2} \sin^2 \alpha + n_{ff}^{-2} \cos^2 \alpha)^{-½}$. However, one can derive the simpler, approximate equation $\Delta n \approx (n_{cc} - n_{ff})\cos^2 \alpha$ for the phase difference if one makes the assumption that the two RIs of the block of white matter are very similar in value i.e., $n_{cc} - n_{ff} << ½(n_{cc} + n_{ff})$.

Methods of PLI

Polarized light is widely used for imaging biological specimens (Scheuner and Hutschenreiter, 1972), and its particular usefulness for visualizing nerve fibers has been known for approximately a century (Göthlin, 1913; Kretschmann, 1967; Schmidt, 1923, 1924; Schmitt and Bear, 1936; Wolman, 1975). In this context, the function of polarized light was simply to increase the visibility of nerves. Such enhancement of visibility has no utility when studying blocks of white matter, as white matter is all nerves. However, recently our working group has demonstrated another use for polarized light when viewing white matter. It can be used to map the spatially varying within-section orientation, and out-of-section inclination of nerve fibers in gross histological sections (Axer and Graf von Keyserlingk, 2000; Axer et al., 2000, 2001). The preferred method for this uses a pair of polarizers and a quarter-wave plate.

Static Crossed-Polars

The simplest way to detect birefringence in a thin section is to sandwich it between a pair of plane polarizers with perpendicular transmission axes, and to pass unpolarized light through the system. The first polarizer filters the light down to a plane polarized beam, which then passes through the section. If the section is not birefringent then there will be no change in the polarization state of the beam and it will be totally absorbed by the second polarizer. If the section is birefringent it will cause the plane polarized beam to become elliptically polarized, and a fraction of it will then be able to pass through the second polarizer. The intensity of the transmitted light is given by the modified formula of Fresnel (Scheuner and

Hutschenreiter, 1972), which (using the notation introduced before) is $I_{\text{trans}} = I \sin^2 2(\theta - \varphi) \sin^2 \delta/2$, where θ and φ are the orientations of the transmission axis of the first polarizer and the a-axis of the section, respectively, and δ is the phase difference induced by the birefringence. In this simple set-up, any transmitted light indicates birefringence, but an absence of light does not necessarily indicate a lack of birefringence as it may be that $\theta = \varphi$ or $\delta = 2k\pi$. The chance alignment causing $\theta = \varphi$ can be eliminated by changing the orientation of the pair of polarizers, while keeping their transmission axes perpendicular. The possibility that by chance the phase shift is an integer number of wavelengths can be eliminated by using incident light which is a mixture of wavelengths.

Rotating Crossed-Polars

By measuring the transmitted light at several different orientations of the polarizers, the crossed-polar setup can also be used to make quantitative measurements. As the polarizers are rotated the transmitted intensity varies sinusoidally. Minimum transmitted intensity is achieved at the four positions of the crossed-polars where the transmission axes line up with the a- and b-axes of the sample. Unfortunately there is nothing to distinguish between these four cases, so the orientation of the a-direction of the sample can only be determined up to a $\pm 90^\circ$ ambiguity (Fig. 4).

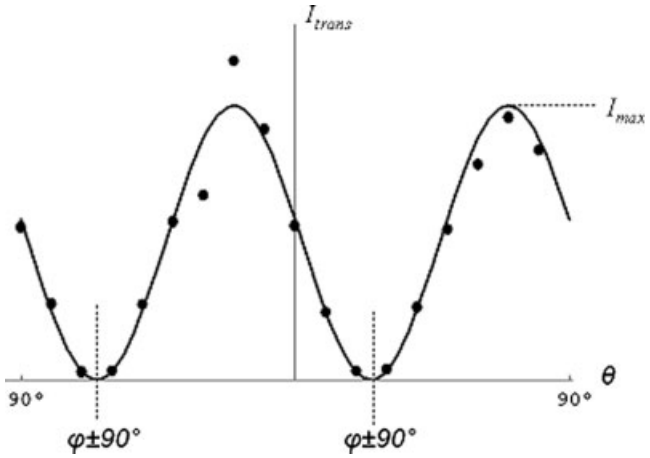

Fig. 4. A sinusoid fitted to noisy intensity data in a crossed-polars setup can be used to recover information about the orientation of the birefringence of the sample. The minimum intensity of transmitted light occurs when one or other of the polar transmission axes are aligned with the fibers in the section. The maximum intensity occurs when the fibers are at 45° to the polar transmission axes.

The sinusoidal variation in transmitted intensity can also be used to estimate fiber inclination. This estimation relies on the three equations: $I_{\max} = I \sin^2 \delta/2$ (for the crossed polar configuration), $\delta = 2\pi\lambda^{-1} t\, \Delta n$ (for the phase shift induced by a birefringent section) and $\Delta n \approx (n_{\text{cc}} - n_{\text{ff}}) \cos^2 \alpha$ (for the difference in refractive indices as a function of fiber inclination). Figure 5 shows how the maximum transmitted intensity varies with fiber inclination, and how this relationship changes depending on the section thickness.

The figure shows that is important not to have the section too thick or the sectioning angle cannot unambiguously be inferred from $I_{\max}$. The thickest section such that there is an unambiguous monotonic relationship is when $t = \frac{1}{2}\lambda(n_{\text{cc}} - n_{\text{ff}})^{-1}$. At this thickness, fibers lying completely within the section act as a half-wave retarder. Even at optimum thickness, the relationship between inclination and maximum intensity is not linear, and it is clear that the accuracy with which inclination can be estimated will be greatest for inclinations between 30 and 60°. For thicknesses thinner than the optimum we see two effects. The first is that maximum transmitted intensities fall for all inclinations. The second is that the range of inclinations for which estimation is most precise shifts downwards.

Figure 6 shows experimental intensity measurements taken using the crossed polars setup for different thicknesses of rat brain section. This figure shows that as the section thickness increases (from the left 20, 30, 40, and 60 μm) the amplitude of measured light also increases.

Rotating Quarter-Wave Plate Plus Crossed-Polars

The ambiguity that occurs with the crossed-polars set-up can be eliminated by the addition of a quarter-wave plate into the set-up. A quarter-wave plate is a standard optical component made of a birefringent medium of thickness such that the plate induces a quarter-cycle phase shift between in-phase beams polarized in its principal planes. The quarter-wave plate is inserted between the polarizer and the section, and is aligned so that its principle axes coincide with the transmission axes of the crossed-polars. Note that there are two ways that the quarter-wave plate can be thus aligned.

The effect of the quarter-wave plate is to transform the plane-polarized light from the polarizer into circularly polarized light. When the circularly polarized light passes through the birefringent sample it is

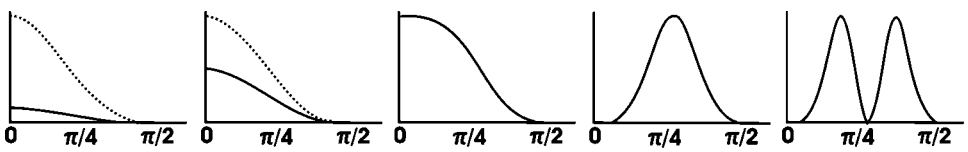

Fig. 5. Shows, for the crossed polar set-up, the relationship between fiber inclination (α) plotted horizontally and the maximum intensity of transmitted light (which occurs when the polar transmission axes are at 45° with the fibers in the section) plotted vertically. The middle plot is for optimum section thickness. From left-to-right, the plots are for thicknesses x¼,x½,x1,x2,x4 compared to the optimum. The solid lines are plotted using the same vertical scale for each panel. The dotted lines are rescaled versions of the solid lines, plotted so that the differences in form compared to the middle plot can more easily be seen.

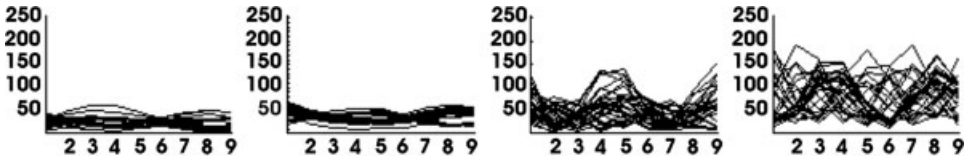

Fig. 6. Measured intensities for rat brain sections in thicknesses of 20, 30, 40, and 60 μm. Measurements were taken with crossed polars only. The intensity (plotted vertically) was measured in 9 different orientations of the polarizers (plotted horizontally) and for clarity is shown only for the most birefringent structures within the sample. The amplitude of measured light increases with the section thickness as predicted by the model.

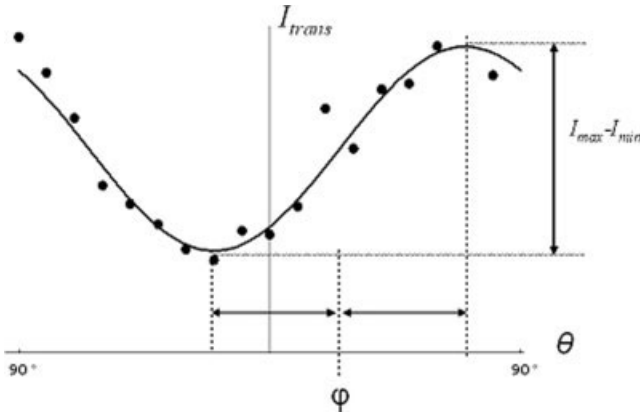

Fig. 7. A sinusoid fitted to noisy intensity data in a quarter-wave plate + crossed-polars setup can be used to recover information about the orientation of the birefringence of the sample. The maximum intensity of transmitted light occurs when the fast axis of the quarter-wave plate is aligned with the fibers in the section, the minimum when these are perpendicular. The fibers are aligned with the axis of the first polar when the intensity is at the midrange value. The figure can be compared with Figure 4, where the same underlying fiber orientation (25°) was used.

transformed into elliptically polarized light. A fraction of this elliptically polarized light then passes through the analyzer; where the fraction transmitted depends on the orientation of the ellipse relative to the axis of the polar. Application of Jones calculus to analyzing this system allows derivation of the following formulae for the transmitted light: $I_{\text{trans}} = \frac{1}{2}I(1 + \sin\delta \sin 2(\theta - \varphi))$, where as before θ and φ are the orientations of the transmission axis of the first polarizer and the *a*-axis of the section, respectively, and δ is the phase difference determined by the birefringence and thickness of the section. Note that if the quarter-wave plate is inserted into the apparatus at the other possible alignment such that its principal axes coincide with the crossed polars, then the equation would be $I_{\text{trans}} = \frac{1}{2}I(1 - \sin\delta \sin 2(\theta - \varphi))$.

As with rotating crossed-polars, when using the quarter-wave plate, data is collected at various orientations and is then fitted to recover the within-section fiber orientation (Fig. 7). Because both the birefringent tissue parts and the quarter-wave plate act as a retardation element on the light wave the position of the quarter-wave plate before (as in the Metripol system) or behind the sample (as in the other polarization system) is not critical.

Use of the quarter-wave plate does not prevent estimation of fiber inclination, but now the estimation is based on the range of transmitted intensities rather than the maximum. From the transmission formulae we arrive at: $I_{\max} - I_{\min} = I \sin\delta$. Figure 8 shows the relationship between the inclination and the range of transmitted intensities. The figure shows that, as with crossed-polars alone, the relationship depends on the section thickness. In contrast with crossed-polars alone, the thickest section such that the relationship is monotonic, is such that completely in-section fibers act as a quarter-wave plate. Thus the optimum thickness when using the quarter-wave plate is half that of using the crossed-polars alone. Using thinner sections has the same advantages and disadvantages as was noted for the crossed-polar set-up. Experimental intensity measurements for different thicknesses of rat brain section taken using the crossed polars setup with inserted quarter wave plate are shown in Figure 9. Compared to Figure 6 which shows the intensity measured for the same sections but without the quarter wave plate, the amplitude of measured light also increases with section thickness but to a lesser extent.

Equipment for PLI of White Matter

We have used two set-ups for acquiring polarized light images. The first system was constructed for this particular purpose, while the second is the commercially available Metripol polarized light microscopy system. The systems are complementary as they allow different magnifications and fields of view.

The system we constructed (Fig. 10) consists of a pair of horizontally mounted crossed-polars and a removable quarter-wave plate. Light is passed through the system from below. The transmitted light is imaged by a downwards pointing CCD camera. This system allows the filters to be rotated while keeping their relative orientation constant, and keeping the sample fixed. The advantage of rotating the filters rather than the sample is that the images collected at different orientations are in perfect register, so the variation of intensity at any particular location of the sample is trivial to extract.

The components of the system were as follows. The light source was five fluorescent tubes (Osram GmbH, München, Germany, 13W, diameter 16 mm, color 25: Universal White). These tubes were parallel-mounted behind a diffusing screen, giving a uniform diffuse broad-band illuminant. The filters used were from B&W Filter, Schneider, Bad Kreuznach, Germany. The CCD camera was the Axiocam HR (Carl Zeiss, Göttingen, Germany), which has a basic resolution of 1300 × 1030 pixel, enhanceable to 3900 × 3090 pixel. The

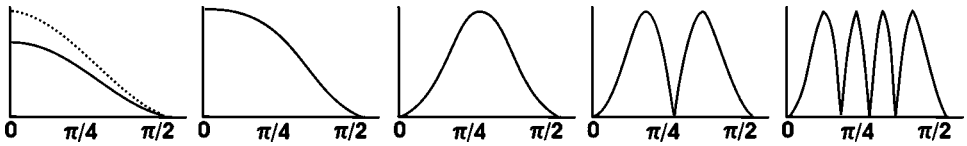

Fig. 8. Shows, for the quarter-wave plate + crossed-polars setup, the relationship between fiber inclination (α) plotted horizontally and the range of transmitted intensities plotted vertically. The different plots are for different section thicknesses: the same thicknesses as in Figure 5. As in Figure 5, the solid lines are plotted using the same vertical scale for each panel, and the dotted line is a rescaled version.

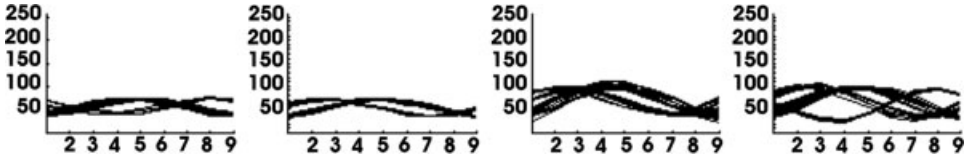

Fig. 9. Measured intensities for rat brain sections in thicknesses of 20, 30, 40, and 60 μm. Measurements were taken for the same sections as in Figure 6 but with inserted quarter wave plate. As in Figure 6 the intensity (plotted vertically) was measured in nine different orientations of the polarizers (plotted horizontally) and for clarity is shown only for the most birefringent structures within the sample.

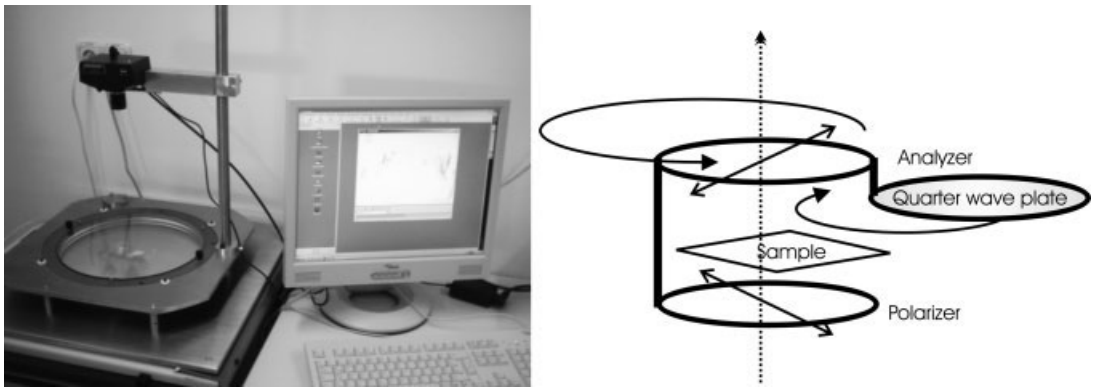

Fig. 10. The principle of polarized light imaging is shown on the right. The polarizer is located before the sample and the analyzer behind the sample. Between sample and analyzer the quarter wave plate can be introduced into the light beam (as per the arrow). The set-up as used in this study is shown on the left.

images were acquired using the AxioVision software (Carl Zeiss, Göttingen, Germany) running on a Windows 2000 operating system on a Pentium PC. It is notable that none of these components is especially high-end, and yet the variation of intensity with filter orientation is clearly visible to the unaided eye and easily recorded by the camera.

The second system that we have used is the Metripol polarizing microscope system (Glazer et al., 1996) developed by the Ferraris Group and produced and marketed by Oxford Cryosystems. The Metripol system can be purchased complete or can be attached to any standard laboratory microscope. In configuration it is similar to our purpose-built system, but with three additions. First, interference filters may be used to create narrow-band illumination from a tungsten-halide lamp. Second, microscope optics between the section and the quarter-wave plate greatly increase the magnification. Third, the system incorporates stepper-motor control of the filter orientation, allowing images to be collected rapidly and precisely at many orientations.

RESULTS

In the following two sections we present results of PLI applied to the human and rat brain. The purpose-built system with a large field-of-view is applied to the human brain, and the commercial system, with a smaller field-of-view but higher magnification, is applied to the rat brain.

Human Brain

Initially this PLI method was developed for imaging fiber orientation in the human brain. The method was applied to serial sections of different anatomical regions of the human brain. All brains were obtained from subjects who donated their bodies for anatomical study. Human cadaver brains were fixed in formalin and macroscopically dissected according to the region of interest. Afterwards, the specimens were serially sectioned with a cryostat microtome CM3050 S (Leica Microsystems, Bensheim, Germany) at a thickness of

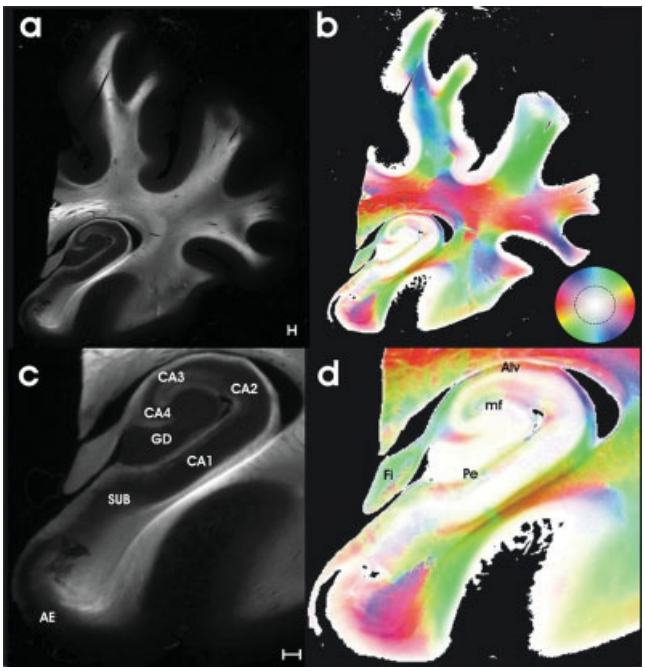

Fig. 11. Frontal section through the human temporal pole including the hippocampal formation. (**a**) and (**c**) are maximum intensity maps which show the maximum intensity of the polarization sequence. (**b**) and (**d**) are fiber orientation maps with color codes for fiber orientation and saturation codes for inclination (inset key). The dashed circle on the inset key roughly indicates 45° inclination. Fibers that are more steeply inclined than this are very pale colored. Abbreviations are: AE, entorhinal area i.e., parahipocampal gyrus; SUB, subiculum; GD, dentate gyrus; CA1–CA4, hippocampal areas; Pe, perforant pathway; mf, mossy fibers; Alv, alveus; Fi, fimbria fornicis; scalebar: 1 mm.

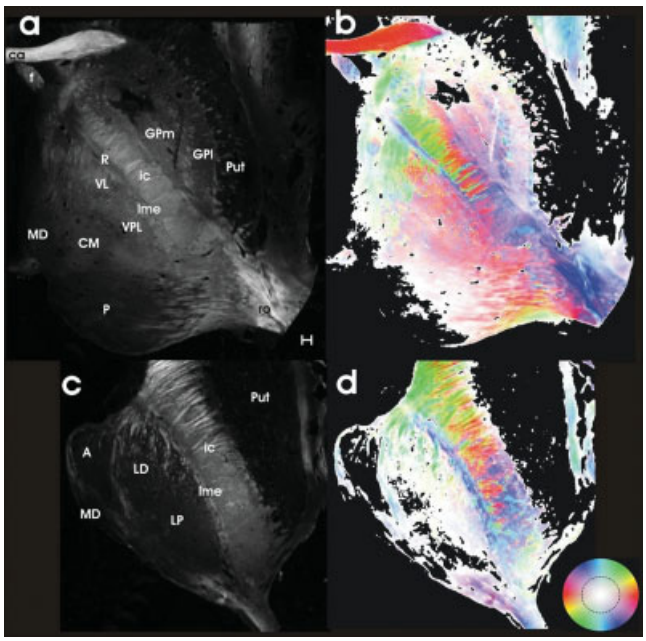

Fig. 12. Horizontal section through the human thalamus. (**a**) and (**c**) show maximum intensity maps. (**b**) and (**d**) are fiber orientation maps with color codes for fiber orientation and saturation codes for inclination (inset key). Abbreviations are: ca, anterior commissure; ic, internal capsule; f, fornix; lme, lamina medullaris externa; ro, optic radiation; GPm, medial globus pallidus; GPl, lateral globus pallidus; Put, putamen thalamic nuclei; A, anterior; CM, centromedian; LD, lateralis dorsalis; LP, lateral posterior; MD, dorsomedial; P, pulvinar; R, reticular; VL, ventralis lateralis; VPL, ventralis posterior lateralis; scalebar: 1 mm.

100 μm. The magnification of the system was such as to result in pixels of dimension $(64\ \mu m)^2$ (i.e., slightly less than the section thickness). For each section, nine images separated by 10° rotations of the filters using polars only and nine images separated by 20° rotations of the filters using an introduced quarter-wave plate were acquired. Sinusoids were fitted to the nine intensity values at each pixel to recover direction (in-plane orientation) and inclination (out-of-plane orientation) information. Figure 11 shows some of the results of processing the data for a frontal section of the temporal pole.

Figures 11a and 11c show the maximum intensity maps, which represent the maximum light intensity of the polarization sequence. These maps yield an image which is comparable to a myelin-stained section. Figures 11b and 11d show fiber orientation maps of the section. The color-coding we have used allows the 3D orientation (i.e., direction and inclination) to be judged from a single image.

Fiber direction is represented as color codes, e.g., red color represents fibers with direction east-west or west-east (see the inset key in Figs. 11 and 12). Inclination is represented as saturation codes, i.e., colors turn paler the steeper the fibers are. In contrast "white" represents tissue without myelin contrast in PLI, i.e.,

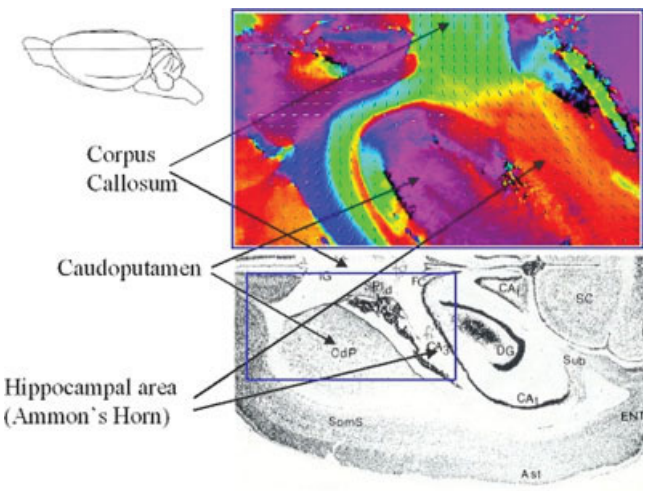

Fig. 13. Axon orientation imaged using the Metripol system in a 60 μm thick trans-axial slice of rat cerebrum. We have hand registered with a plate from a standard rat atlas (Cui and Lawrence, 1995)—the blue frame overlay on the lower panel shows the field of view of the upper panel. The overlaid lines in the top panel indicate orientation and are spaced at 150 μm intervals.

gray matter in most of the cases. Considerable components, which show up in "white" or very pale colors relate to gray matter, which itself is shown in very dark gray in the maximum intensity images (Figs. 11a and 11c and 12a and 12c).

In the case of the hippocampal formation (Fig. 11), a fiber loop can be seen in the maps consisting of the perforant pathway (connecting the entorhinal area with the dentate gyrus), the mossy fiber system (the projection from the dentate gyrus to the hippocampal areas CA3 and CA4), and the alveus (the efferents of the areas CA1 to CA4 running into the fornix fiber system).

Although the method was developed to calculate fiber orientation in the white matter of the human brain, the method also yields information about gray matter anatomy. Figure 12 shows two horizontal sections through the human thalamus. Besides white matter fiber orientation (anterior commissure, fornix, internal capsule, optic radiation), the thalamic subnuclei can be differentiated. Moreover, the thalamic subnuclei also show distinct fiber orientation anatomy. Because gray matter tissue consists of different contents of myelinated fibers, the fiber inclination angles in gray matter cannot be reliably estimated using the same imaging settings (contrast, brightness) as used here, but this may be feasible by changing the sensitivity and magnification of the imaging system.

Rat Cerebrum

We have applied the PLI technique to rat brains perfused with paraformaldehyde and sectioned using a cryostat. As rat brains are smaller than human brains it is easier to obtain and handle thin sections. This is significant as it is easy to obtain images with in-plane sample spacing, which is finer than the slice thickness, so it is slice thickness which determines the upper-bound of isotropic 3D resolution obtainable with PLI. Using the Metripol system we have been able to obtain a birefringence signal from sections as thin as 20 μm, though for ease of handling we typically use 60 μm thick sections.

The results we have obtained match the known anatomy (Fig. 13) confirming that although the PLI method has been developed using human brain material, it applies unaltered to the rat brain.

The Metripol system is built around a microscope so it is easy to perform PLI at different magnifications. We have used this facility to test our expectation that section thickness determines the resolution of the orientation image that can be measured. Figure 14 shows images obtained at different magnifications and overlapping fields of view. One image has $(10\ \mu m)^2$ pixels and the other $(1.6\ \mu m)^2$. We would expect that since the larger pixel size is already smaller than the section thickness, no extra structure will be visible using the smaller pixels. And this is what we see in practice.

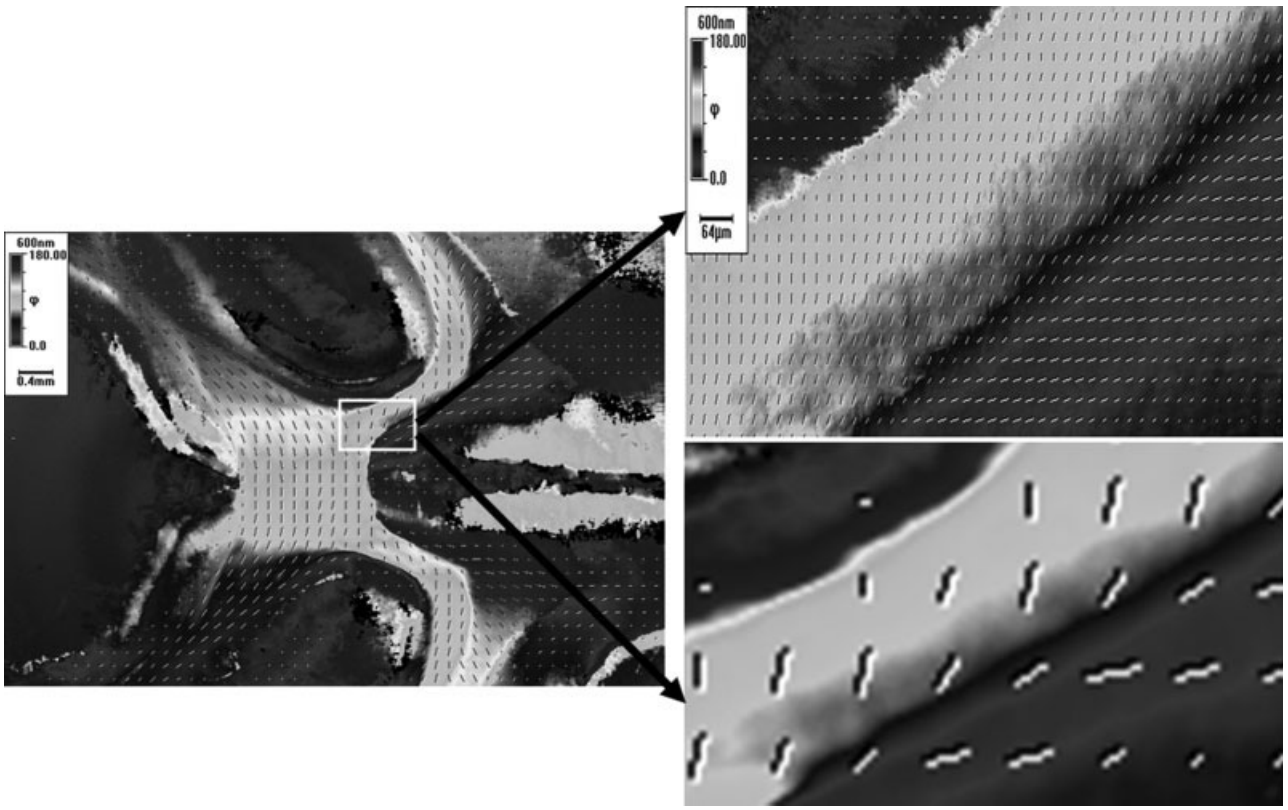

Fig. 14. The left image has $(10\ \mu m)^2$ pixels. The bottom right image shows an expanded view of the area marked by the rectangle. The top-right image is a different image of the same area of interest but acquired at a higher magnification so that its pixels are $(1.6\ \mu m)^2$ in size. The bars in the keys of the two uppermost images show the linear size of the images, which can be compared with the 60 μm section thickness.

TABLE 1. Comparison of DT-MRI and PLI

	PLI (Birefringence)		DT-MRI (Diffusion)	
Physical principle	Rat brain PLI	Human brain PLI	Conventional DT-MRI	Microscopy DT-MRI
Best anisotropic resolution		$(60\ \mu m)^2 \times 100\ \mu m$		9.4T: $(39\ \mu m)^2 \times 156\ \mu m$ (DWI) 3T: $(300\ \mu m)^2 \times 1200\ \mu m$
Best isotropic resolution	$(60\ \mu m)^3$	$(100\ \mu m)^3$	1.5T: $(2.5mm)^3$	9.4T: $39\ \mu m \times 47\ \mu m \times 47\ \mu m$
Field of view	Whole brain imaging possible		Whole brain imaging possible	Limited field of view makes whole brain imaging impossible
2D vs. 3D	Inclination ambiguity. Difficult to assemble section data into 3D		Data is reliably 3D	

DISCUSSION

Neuroanatomists have been making maps of white matter architecture for more than a century and several methods have now been developed. The methods rely on an impressive diversity of physical principles. The earliest was application to brain sections of the Weigert myelin-selective stain (Dejerine, 1901; Vogt, 1902). Later came the macroscopic dissection technique of Klingler (Ludwig and Klingler, 1956) who showed that repeated freezing of brains causes ice crystals to grow that naturally separate nerve fibers. Next, and still actively being developed, came methods that exploit active transport mechanisms in axons to determine nerve fiber connections in living animals (Borcard and Legendre, 2002; Heimer and Robards, 1982; Lanciego and Wouterlood, 2000). Passive transport along axons in postmortem tissue has also been demonstrated (Sparks et al., 2000), but only over inconveniently long timescales.

The development of MR diffusion tensor imaging in recent years has been widely and rightly hailed as a major advance in this field. However the resolution obtainable by DT-MRI is coarser than the target resolution of $(10\ \mu m)^3$ that is necessary for the unambiguous mapping of fiber architecture. Now attention is turning to extensions of DT-MRI such as diffusion spectrum imaging (DSI) (Chen et al., 2004; Does et al., 2003; Gilbert et al., 2004) that aim to "see inside" individual voxels and thus attain the desired resolution.

The resolution of MRI has been steadily improved since the invention of the method. The resolution obtainable using standard equipment is now of the order of $(2.5\ mm)^3$. There do exist dedicated and expensive scanners specially built for high resolution imaging, incorporating components such as high-field superconducting magnets, microfrequency coils, and strong gradients. However, these require prolonged scanning of small samples of unmoving tissue, which must therefore by necessity be post mortem. The use of postmortem tissue is a problem for DT-MRI. Some DT-MRI studies have been unsuccessful in measuring diffusion in fixed tissue (Kier et al., 2004; Pfefferbaum et al., 2004). Other studies have found a reduced signal because water diffusion decreases 50–75% in fixed tissue (Sun et al., 2003). However, several DT-MRI studies on postmortem brain tissue exist (Ahrens et al., 1998; Englund et al., 2004; Jacobs et al., 1999; Larsson et al., 2004; Mori et al., 1999, 2001). In the literature the terms MRM (MR microscopy) (Benveniste and Blackband, 2002), μMR (Chin et al., 2004), and MRH (MR histology) (Johnson et al., 1993) are used to describe high resolution MR. High resolution MR generally refers to a voxel size of less than 100 μm in at least one direction. The best resolution claimed for DT-MRI is $39 \times 47 \times 47\ \mu m^3$ on post mortem mouse brain with a 9.4T scanner (Mori et al., 2001).

Table 1 gives an overview of some characteristics of PLI and DT-MRI. Although MRI images may be mildly spatially deformed, these deformations are of low spatial frequency—hence neighboring voxels really do correspond to neighboring volumes of tissue. In contrast, in PLI the distortions that result when we align sections into a 3D volume can be of high frequency. So a resolution of $(20\ \mu m)^3$ across a volume (rather than a single section), while possible, has not yet been achieved. While we expect to improve sectioning and alignment methods, it is unlikely that these can ever be made good enough to realize the full resolution potential of PLI.

Although the results of PLI (Figs. 11–13) are presented as 2D images composed of 2D pixels, in fact, due to the nonzero thickness of the imaged sections, they can equally be regarded as 2D images composed of 3D voxels. Each pixel/voxel is an estimate of the orientation and inclination of the fibers in a small cuboid of white matter. Because white matter fibers run in such a variety of directions, all three dimensions of the cuboid are of equal significance, and so the effective isotropic resolution is determined by the longest of the three dimensions.

Thus, the resolution of the method depends on three factors, the magnification of the image capture system (camera lens or microscope), the resolution of the imaging system (e.g., 1300×1030 pixels), and the thickness of the section. Although the limiting factor on the resolution can in principle be either the in-plane pixel size or the section thickness, in practice we have been able to achieve sufficiently small pixel size so that the section thickness is the limiting factor.

So to maximize resolution we need to use sections as thin as possible. Several factors limit how thin the sections can be. The first is that thinner sections give a lower amplitude variation with orientation in intensity, requiring a more precise imaging system. The second is that with thinner sections, estimation of fiber parameters for fibers of inclination near normal becomes especially imprecise. The third is that thinner sections are more difficult to section intact consistently, leading to missing sections out of a 3D volume. The fourth is that thinner sections distort more, so reconstruction of a 3D volume is much more difficult.

For our human brain studies we have used the criteria that all inclinations should be equally precisely estimated. This led to us assessing the Pearson correlation

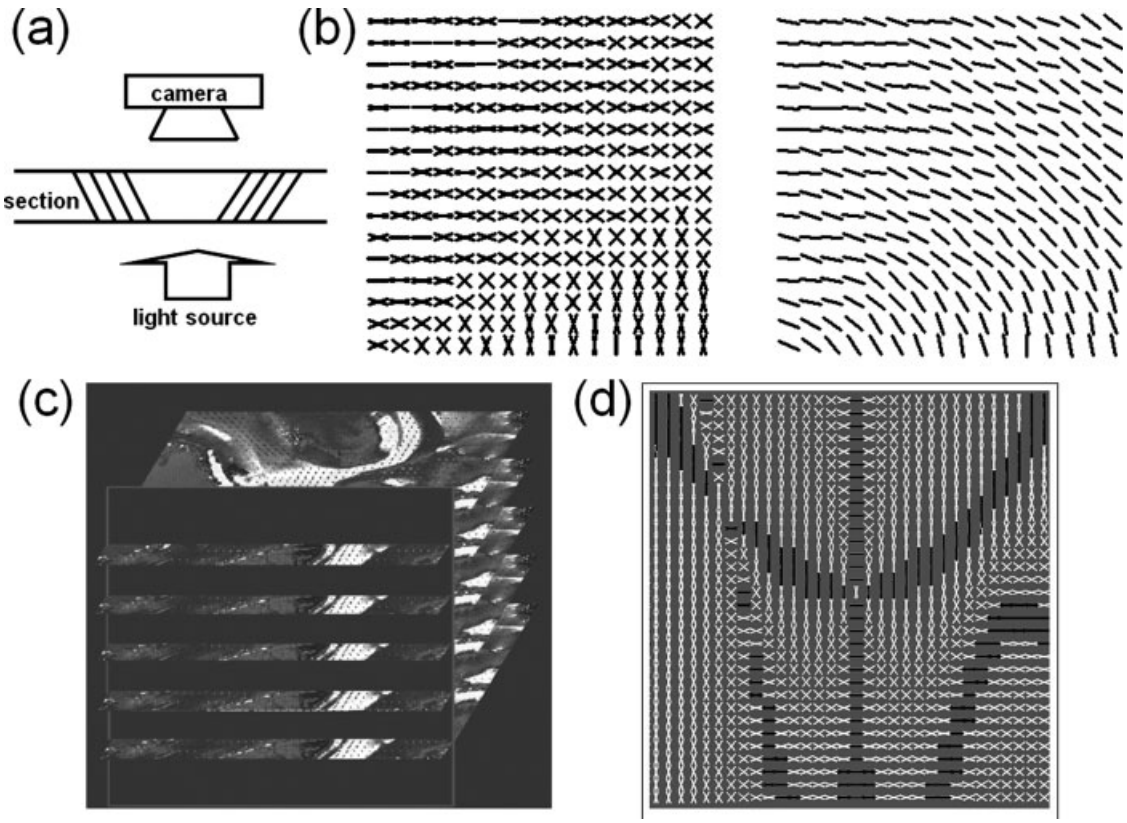

Fig. 15. (**a**) shows the inclination ambiguity. Both populations of fibers have the same within-section orientation and out-of-section inclination, even though they have different 3D orientations. (**b**) to resolve the inclination problem we consider data from adjacent sections. (**c**) each row of the two panels is from a separate section. The left panel shows the two possible 3D orientations, the right panel shows a disambiguation solution found using our continuity heuristic algorithm. (**d**) Shows a 2D slice through a 3D block of data. Each row of the plot comes from a single section. White symbols mark locations where there is inclination ambiguity, black symbols where there is little or no ambiguity.

coefficient between sinusoid amplitude and inclination for different section thicknesses. We found that the correlation was maximized for thicknesses between 80 and 120 μm (Axer et al., 2001), and so settled on 100 μm for our studies. For our rat brain studies we adopted a different strategy and instead assessed the thinnest section that allowed us to produce a birefringence signal strong enough to be captured by the Metripol system. We were able to image sections as thin as 20 μm. However, at this thickness we found that the practical problems of cutting and handling thin sections were intrusive, and so opted instead for 60 μm for our main studies. We conclude that the limiting factor for the resolution obtainable by PLI is the difficulty of sectioning and handling thin sections.

Sixty micrometer resolution is an order of magnitude larger than typical fiber diameters, so it seems likely that PLI will also have to cope with some pixels containing fibers at several orientations. This is unavoidable. Even if fibers are organized into tracts of hundreds of fibers, there will be some pixels that overlap multiple tracts. For such pixels, the orientation estimate will be erratic and unreliable, and there will be a tendency to over-estimate the inclination as a sum of equal-frequency sinusoids of different phase will have a lower amplitude than the individual sinusoids.

Although PLI can recover within-section orientation and out-of-section inclination, this is insufficient to completely estimate the 3D orientation of fibers. The problem is that for most inclinations there are two possible 3D orientations that are consistent within the measurements. The problem is most acute for intermediate inclinations such as 45° where the possible 3D orientations are actually at 90° to each other (Fig. 15a). For fibers perfectly in the section or normal to it, there is no inclination ambiguity.

This inclination ambiguity is not particularly serious when we visualize the results of PLI on a single section (e.g., Fig. 11), but is a problem when we attempt to assemble multiple sections into a 3D volume. In such a case we would like to recover a full 3D array of 3D fiber orientations, so that we can perform tract tracing (Ffytche and Catani, 2005; Kanaan et al., 2005). Figures 15b and 15c illustrate the problem.

To resolve the inclination ambiguity we need, at each location, to select one of the two possible 3D orientations. As a method of guiding these selections, we have proposed to make use of the following continuity heuristic (Larsen and Griffin, 2004): spatial variation in fiber orientation is more likely to be slow than fast. Thus we can select, at each location, one of the two possible orientations so that over the entire reconstructed

volume the 3D orientation varies as smoothly as possible. Figure 15c shows an example of the result of applying this heuristic. This result was found using a simulated annealing algorithm applied to a quadtree representation of the problem.

Although the method appears successful, further investigation revealed an inherent problem that cannot easily be resolved. The difficulty is that for the data shown in Figure 15d, there is an alternative solution that is completely different but just as smooth as the one found. In this alternative solution, each local inclination decision is the opposite to the one shown, this results in a pattern of fibers that are generally oriented bottom-left to top right, rather than bottom-right to top-left.

Further analysis shows that these larger scale ambiguities are pervasive but of simple form. Figure 15d shows how blocks of ambiguity are delineated by fibers that have 0 or 90° inclination and so no ambiguity. For each block there are two possible solutions, and the solution in each block is independent of other blocks (Fig. 15d). Thus disambiguation is possible if an external source of data (e.g., a neuroanatomist) makes one decision per block. Though this is much easier than making a decision at every pixel, even this task in the presence of noise is tedious and difficult.

RI is not the only tensor-valued physical parameter that correlates with white matter fiber orientation: diffusivity (Basser et al., 1994) and impedance (Axer et al., 1999) are similarly related. In fact, a theoretical model has been presented that predicts that the tensors of all transport phenomena in white matter should agree in orientation (Tuch et al., 2001). Of the various physical parameters, diffusivity has received the most attention as the basis of an imaging method because it can be measured in the unsectioned brain using a variant of magnetic resonance imaging technology known as DT-MRI (Basser et al., 1994).

As DT-MRI data is three-dimensional another focus was also given to the development of three-dimensional PLI atlas of the human brainstem. In total, each brainstem (from medulla oblongata up to the diencephalon) produced about 1,200 sections, and every second section was polarized light imaged. The fiber orientation maps of the brainstem sections were assembled into a 3D volume. This was accomplished using an image registration algorithm that finds the rigid transformation between two adjacent slices that minimizes the summed squared pixel difference between the slices (Axer et al., 2002). Having aligned the data into a volume, fiber tracts can manually be outlined by a neuroanatomist. However, any 3D reconstruction of PLI data from multiple cross-sections opens up a new field of problems not really associated with the PLI technique but with issues of tissue preparation and/or computer modeling. Thus, these issues are outside the scope of this article.

PLI is yet another technique for mapping fiber architecture, based on yet another physical principle. Like all methods it has its strengths and weaknesses. Its strength is the high resolution that can be obtained in individual brain sections. Its weaknesses are that it is only applicable to postmortem tissue, it suffers from an intrinsic ambiguity, which means that full 3D orientation is not recoverable, and the 3D resolution that can be obtained by assembling multiple sections is far poorer than that of individual sections. It has obvious potential for the validation and calibration of DT-MRI and DSI techniques, an enterprise that has been started (Lin et al., 2003) but still needs further research (Kinoshita et al., 2005); but it also has potential for niche applications such as animal studies (e.g., stem cell migration) and detailed mapping of specific structures (e.g., brain stem). Finally, if a reflected rather than transmitted light variant can be developed, mapping at the target $(10\ \mu m)^3$ resolution should be possible, a prospect that seems unlikely for MRI-based techniques.

ACKNOWLEDGMENTS

We would like to thank Daniela Hoffmann, Simone Böhm, and Claudia Doering from the Department of Neurology in Jena for their technical assistance. Special thanks to Oxford Cryosystems, Klaus Qvortrup, Susan Peters, and Mary-Ann Gleie at the Department of Medical Anatomy, The Panum Institute, Copenhagen, for their help.

REFERENCES

Ahrens ET, Laidlaw DH, Readhead C, Brosnan CF, Fraser SE, Jacobs RE. 1998. MR microscopy of transgenic mice that spontaneously acquire experimental allergic encephalomyelitis. Magn Reson Med 40:119–132.

Axer H, Graf von Keyserlingk D. 2000. Mapping of fiber orientation in human internal capsule by means of polarized light and confocal scanning laser microscopy. J Neurosci Methods 94:165–175.

Axer H, Stegelmeyer J, Graf von Keyserlingk D. 1999. Comparison of tissue impedance measurements with nerve fiber architecture in human telencephalon: Value in identification of intact subcortical structures. J Neurosurg 90:902–909.

Axer H, Berks G, Graf von Keyserlingk D. 2000. Visualization of nerve fiber orientation in gross histological sections of the human brain. Microsc Res Tech 51:481–492.

Axer H, Axer M, Krings T, Graf von Keyserlingk D. 2001. Quantitative estimation of 3D fiber course in gross histological sections of the human brain using polarized light. J Neurosci Methods 105:121–131.

Axer H, Leunert M, Murkoster M, Gräβel D, Larsen L, Griffin LD, Graf von Keyserlingk D. 2002. A 3D fiber model of the human brainstem. Comput Med Imaging Graph 26:439–444.

Basser PJ, Mattiello J, LeBihan D. 1994. Estimation of the effective self-diffusion tensor from the NMR spin echo. J Magn Reson B 103:247–254.

Beaulieu C. 2002. The basis of anisotropic water diffusion in the nervous system—A technical review. NMR Biomed 15:435–455.

Benveniste H, Blackband S. 2002. MR microscopy and high resolution small animal MRI: Applications in neuroscience research. Prog Neurobiol 67:393–420.

Beuthan J, Minet O, Helfmann J, Herrig M, Muller G. 1996. The spatial variation of the refractive index in biological cells. Phys Med Biol 41:369–382.

Borcard D, Legendre P. 2002. All-scale spatial analysis of ecological data by means of principal coordinates of neighbour matrices. Ecol Model 153:51–68.

Chen JH, Chen H, Yen CT. 2004. High-field MRI of brain activation and connectivity. Chin J Phys 42:520–525.

Chin CL, Wehrli FW, Fan YL, Hwang SN, Schwartz ED, Nissanov J, Hackney DB. 2004. Assessment of axonal fibre tract architecture in excised rat spinal cord by localized NMR q-space imaging: Simulations and experimental studies. Magn Reson Med 52:733–740.

Cui Y, Lawrence PD. 1995. Detecting scale-space consistent corners based on corner attributes. In: IEEE International conference on systems, man and cybernetics, Vol. 4. Vancouver, BC: Canada. pp.3549–3554.

de Campos Vidal B, Mello ML, Caseiro-Filho AC, Godo C. 1980. Anisotropic properties of the myelin sheath. Acta Histochem 66:32–39.

Dejerine J. 1901. Anatomie des centres nerveux. Paris: Rueff.

Does MD, Parsons EC, Gore JC. 2003. Oscillating gradient measurements of water diffusion in normal and globally ischemic rat brain. Magn Reson Med 49:206–215.

Englund E, Sjobeck M, Brockstedt S, Latt J, Larsson EM. 2004. Diffusion tensor MRI post mortem demonstrated cerebral white matter pathology. J Neurol 251:350–352.
Ffytche DH, Catani M. 2005. Beyond localization: From hodology to function. Philos Trans R Soc Lond B Biol Sci 360:767–779.
Fraher JP, MacConaill MA. 1970. Fiber bundles in the CNS revealed by polarized light. J Anat 106:170.
Gilbert RJ, Napadow VJ, Weeden VJ. 2004. Determination of lingual myoarchitecture with high angular resolution by diffusion spectrum imaging. Gastroenterology 126 (Suppl 2):A200.
Gimpel JA, Lahpor JR, Vandermolen AJ, Damen J, Hitchcock JF. 1995. Reduction of reperfusion injury of human myocardium by allopurinol—A clinical-study. Free Radic Biol Med 19:251–255.
Glazer AM, Lewis JG, Kaminsky W. 1996. An automatic optical imaging system for birefringent media. Proc Math Phys Eng Sci 452:2751–2765.
Göthlin G. 1913. Die doppelbrechenden Eigenschaften des Nervengewebes. Uppsala: Friedländer & Sohn.
Griffin LD. 1994. The intrinsic geometry of the cerebral-cortex. J Theor Biol 166:261–273.
Haskell RC, Carlson FD, Blank PS. 1989. Form birefringence of muscle. Biophys J 56:401–413.
Heimer L, Robards M. 1982. Neuroanatomical tract-tracing methods. New York: Plenum.
Hoyt CC, Oldenbourg R. 1999. Structural analysis with quantitative birefringence imaging. Am Lab 31:34.
Jacobs RE, Ahrens ET, Dickinson ME, Laidlaw D. 1999. Towards a microMRI atlas of mouse development. Comput Med Imaging Graph 23:15–24.
Jin LW, Claborn KA, Kurimoto M, Geday MA, Maezawa I, Sohraby F, Estrada M, Kaminsky W, Kahr B. 2003. Imaging linear birefringence and dichroism in cerebral amyloid pathologies. Proc Natl Acad Sci USA 100:15294–15298.
Johnson GA, Benveniste H, Black RD, Hedlund LW, Maronpot RR, Smith BR. 1993. Histology by magnetic-resonance microscopy. Magn Reson Q 9:1–30.
Jones DK, Griffin LD, Alexander DC, Catani M, Horsfield MA, Howard R, Williams SCR. 2001. Spatial normalization and averaging of diffusion tensor MRI data sets. Neuroimage 17:592–617.
Jouk PS, Usson Y, Michalowicz G, Parazza F. 1995. Mapping of the orientation of myocardial cells by means of polarized light and confocal scanning laser microscopy. Microsc Res Tech 30:480–490.
Kaminsky W, Claborn K, Kahr B. 2004. Polarimetric imaging of crystals. Chem Soc Rev 33:514–525.
Kanaan RA, Shergill SS, Barker GJ, McGuire PK, Ng VW, Jones DK. 2005. The corpus callosum in schizophrenia examined with DTI tractography. Schizophr Bull 31:393.
Kier EL, Staib LH, Davis LM, Bronen RA. 2004. Anatomic dissection tractography: A new method for precise MR localization of white matter tracts. Am J Neuroradiol 25:670–676.
Kinoshita M, Yamada K, Hashimoto N, Kato A, Izumoto S, Baba T, Maruno M, Nishimura T, Yoshimine T. 2005. Fiber-tracking does not accurately estimate size of fiber bundle in pathological condition: Initial neurosurgical experience using neuronavigation and subcortical white matter stimulation. Neuroimage 25:424–429.
Kretschmann HJ. 1967. [On the demonstration of myelinated nerve fibers by polarized light without extinction effects.] J Hirnforsch 9:571–575.
Lai JC, Li ZH, Wang CY, He AZ. 2005. Experimental measurement of the refractive index of biological tissue's by total internal reflection. Appl Opt 44:1845–1849.
Lanciego JL, Wouterlood FG. 2000. Neuroanatomical tract-tracing methods beyond 2000: What's now and next. J Neurosci Methods 103:1–2.
Larsen L, Griffin LD. 2004. Can a continuity heuristic be used to resolve the inclination ambiguity of polarized light imaging? In: Sonka M, Kakadiaris IA, Kybic G, editors. Computer vision and mathematical methods in medical and biomedical image analysis. Berlin: Springer. pp. 365–375.
Larsson EM, Englund E, Sjöbeck M, Lätt J, Brockstedt S. 2004. MRI with diffusion tensor imaging post-mortem at 3.0 T in a patient with frontotemporal dementia. Dement Geriatr Cogn Disord 17:316–319.
Lin CP, Wedeen VJ, Chen JH, Yao C, Tseng WYI. 2003. Validation of diffusion spectrum magnetic resonance imaging with manganese-enhanced rat optic tracts and ex vivo phantoms. NeuroImage 19:482–495.
Ludwig E, Klingler J. 1956. Atlas cerebri humani. Basel: Karger.
Mesulam M-M. 1990. Large-scale neurocognitive networks and distributed processing for attention, language and memory. Ann Neurol 28:597–613.
Miklossy J, Vanderloos H. 1991. The long-distance effects of brain-lesions—Visualization of myelinated pathways in the human brain using polarizing and fluorescence microscopy. J Neuropathol Exp Neurol 50:1–15.
Morell P, Quarles RH, Norton WT. 1989. Formation, structure and biochemistry of myelin. In: Siegel G, Agranoff B, Albers W, Molinoff P, editors. Basic neurochemistry. New York: Raven Press. pp. 109–136.
Mori S, Crain BJ, Chacko VP, van Zijl PCM. 1999. Three-dimensional tracking of axonal projections in the brain by magnetic resonance imaging. Ann Neurol 45:265–269.
Mori S, Itoh R, Zhang JY, Kaufmann WE, van Zijl PCM, Solaiyappan M, Yarowsky P. 2001. Diffusion tensor imaging of the developing mouse brain. Magn Reson Med 46:18–23.
Oldenbourg R, Mei G. 1995. New polarized-light microscope with precision universal compensator. J Microsc 180:140–147.
Pfefferbaum A, Sullivan EV, Adalsteinsson E, Garrick T, Harper C. 2004. Postmortem MR imaging of formalin-fixed human brain. NeuroImage 21:1585–1595.
Richards AG. 1944. The structure of living insect nerves and nerve sheaths as deduced from the optical properties. J N Y Entomol Soc 52:285.
Scheuner G, Hutschenreiter J. 1972. Polarisationsmikroskopie in der Histophysik. Leipzig: VEB Georg Thieme.
Schmidt W. 1923. Zur Doppelbrechung des Nervenmarks. Zeitschr f wiss Mikroskopie 41:29–38.
Schmidt W. 1924. Die Bausteine des Tierkörpers im polarisierten Lichte. Bonn: Cohen.
Schmitt FO, Bear RS. 1936. The optical properties of vertebrate nerve axons as related to fiber size. J Cell Comp Physiol 9:261–273.
Sparks DL, Lue LF, Martin TA, Rogers J. 2000. Neural tract tracing using Di-I: A review and a new method to make fast Di-I faster in human brain. J Neurosci Methods 103:3–10.
Sun SW, Neil JJ, Song SK. 2003. Relative indices of water diffusion anisotropy are equivalent in live and formalin-fixed mouse brains. Magn Reson Med 50:743–748.
Tower TT, Tranquillo RT. 2001. Alignment maps of tissues. I. Microscopic elliptical polarimetry. Biophys J 81:2954–2963.
Tuch DS, Wedeen VJ, Dale AM, George JS, Belliveau JW. 2001. Conductivity tensor mapping of the human brain using diffusion tensor MRI. Proc Natl Acad Sci USA 98:11697–11701.
Turner A, Chapman D, Penn A. 2000. Sketching space. Comput Graph 24:869–879.
Vogt O. 1902. Neurobiologische Arbeiten. Erste Serie: Beiträge zur Hirnfaserlehre. Jena: Fischer.
Wakana S, Jiang HY, Nagae-Poetscher LM, van Zijl PCM, Mori S. 2004. Fiber tract-based atlas of human white matter anatomy. Radiology 230:77–87.
Weiner O. 1912. Die Theorie des Mischkörpers für das Feld der stationären Strömung. Abhandlungen der Sächsischen Akademie der Wissenschaften. Mathematisch-Physische Klasse 32:507–604.
Wolman M. 1970. On the use of polarized light in pathology. Pathol Annu 5:381–416.
Wolman M. 1975. Polarized light microscopy as a tool of diagnostic pathology. A review. J Histochem Cytochem 23:21–50.